

Global Evaluation of the Precipitable Water Vapor Product from MERSI-II onboard the Fengyun-3D Satellite

Wengang Zhang¹, Ling Wang^{2,3†}, Yang Yu¹, Guirong Xu¹, Xiuqing Hu^{2,3}, Zhikang Fu¹, Chunguang Cui¹

¹Hubei Key Laboratory for Heavy Rain Monitoring and Warning Research, Institute of Heavy Rain, China Meteorological Administration, Wuhan 430205, China

²Key Laboratory of Radiometric Calibration and Validation for Environmental Satellites, China Meteorological Administration, Beijing 100081, China

³National Satellite Meteorological Center, China Meteorological Administration, Beijing 100081, China

Correspondence to: Ling Wang (lingw@cma.cn)

Abstract. The global evaluation of precipitable water vapor (PWV) derived from the advanced Medium Resolution Spectral Imager (MERSI-II) onboard FengYun-3D is performed herein by comparing with the PWV from the Integrated Global Radiosonde Archive (IGRA) based on a total of 462 sites (57,219 match-ups) during 2018–2021. The monthly averaged PWV from MERSI-II presents a decreasing distribution of PWV from the tropics to the polar regions. In general, a sound consistency exists between the PWVs of MERSI-II and IGRA, and their correlation coefficient is 0.951 and root mean squared error (RMSE) is 0.36 cm. The histogram of MB shows that the MB is concentrated around zero and mostly located within the range from -1.00 cm to 0.50 cm. For most sites, the PWV is underestimated with the MB between -0.41 cm and 0.05 cm. However, there is also overestimated PWV, which is mostly distributed in the surrounding area of the Black Sea and the middle of South America. There is a slight underestimation of MERSI-II PWV for all seasons with the MB value below -0.18 cm, with the bias being the largest magnitude in summer. This is probably due to the presence of thin clouds, which weaken the radiation signal observed by the satellite. We also find that there is a larger bias in the Southern Hemisphere, with a large value and significant variation of PWV. The binned error analysis revealed that the MB and RMSE increased with the increasing value of PWV, but there is an overestimation for PWV smaller than 1.0 cm. In addition, there is a higher MB and RMSE with a larger spatial distance between the footprint of the satellite and the IGRA station, and the RMSE ranged from 0.33 cm to 0.47 cm.

1 Introduction

Water vapor is an important component of the atmosphere and widely known as an important greenhouse gas since it can significantly affect climate change, the radiation balance, and the hydrological cycle (Kiehl & Trenberth, 1997; Held & Soden, 2000; Dessler & Wong, 2009; Zhao et al., 2012). The spatiotemporal variations of water vapor are essential for understanding the formation of clouds and mesoscale meteorological systems in that cloud, and precipitation always rely on changes in water

30 vapor (Trenberth et al., 2003). Furthermore, water vapor can also influence the atmospheric transmittance, and the upward
31 radiance measured by the satellite sensor. Therefore, the information of water vapor is highly required to correct atmospheric
32 effects in the satellite-based retrieval algorithm for land surface temperature (Meng et al., 2017).

33 Considering the critical role of water vapor, technologies aiming at the measurement of atmospheric water vapor have
34 been developed. The precipitable water vapor (PWV), which means the integrated water vapor contained in a vertical column
35 of a cross-sectional area, is an important indicator for the total atmospheric water vapor condition. The two major methods
36 used for measuring PWV are satellite-based and ground-based technologies. Several ground-based measurements, such as
37 radiosonde (Durre et al., 2009), global position system (GPS) receivers (Bevis et al., 1992), microwave radiometer (MWR)
38 (Westwater, 1978) and sun photometer (Alexandrov et al., 2009), have been deployed to monitor the variability of water vapor.
39 However, the spatial coverage of ground-based measurements is limited and inhomogeneous, and it is difficult to obtain a wide
40 range of observations from multiple sources to support studies for the distribution of PWV on both a regional and global scale.
41 This is because the uncertainties of different measurements are not completely consistent, and they have distinct discrepancies
42 and magnitudes (Chen & Liu, 2016; Wang et al., 2016). Different from ground-based measurements, the satellite-based
43 measurement is more useful for the temporal analysis of PWV over a wide area. In particular, the polar-orbiting satellite-based
44 measurements of water vapor have a considerable advantage due to their global coverage with satisfactory temporal and spatial
45 resolutions. Therefore, the polar-orbiting satellite-based PWV product is widely used for understanding the global distribution
46 of water vapor. As is commonly known, the well knowledge of global water vapor distribution is especially important for
47 global atmospheric models aiming to predict weather or climate. Thus, the water vapor products retrieved via polar-orbiting
48 satellites have become essential input parameters to sustain numerical models of the atmosphere, especially where global water
49 vapor information is required within a short time span, and the assimilation of PWV has been proven to help improve
50 precipitation forecasts (Rakesh et al., 2009).

51 Over the past few decades, satellite-based PWV retrieval algorithms have been developed with observations from
52 different sensors, which can be divided into four main types according to the spectral region: (1) visible (VIS), (2) near-infrared
53 (NIR), (3) thermal infrared (TIR), and (4) microwave (MW). There are three major satellite-borne sensors that can provide
54 the global NIR PWV product. The Moderate Resolution Imaging Spectroradiometer (MODIS) onboard the Terra and Aqua
55 polar-orbiting satellite platforms is one of the most important instruments for obtaining global PWV, and has been widely used
56 for a few decades since the launching of Terra spacecraft in 1999. The Medium Resolution Imaging Spectrometer (MERIS) is
57 one of ten instruments built in Envisat, which was launched on 1 March 2002, but the mission was terminated on 8 April 2012
58 due to the loss of contact with the satellite. For the Chinese FengYun 3 (FY-3) meteorological series satellite, one of the major
59 payloads onboard is the Medium Resolution Spectral Imager (MERSI), which primarily monitors the ocean, land, atmosphere,
60 etc. FY-3D is the second-generation Chinese polar-orbiting meteorological satellite, equipped with the advanced MERSI
61 (MERSI-II), and was launched on 15 November 2017. For MERIS, the PWV retrieval algorithm employs the ratio of top of

62 atmosphere (TOA) radiance at one water vapor absorption channel (around 900 nm) to the TOA radiance at the atmospheric
63 window channel such as 885 nm (Bennartz and Fischer, 2001). However, both the algorithms for NIR PWV derivation of
64 MODIS and MERSI-II adopt the reflected solar radiance ratios between three NIR water vapor absorption channels and two
65 non-absorption channels (Gao and Kaufman, 2003; Wang et al., 2021). The setup of non-absorption channels of MERSI-II is
66 the same as that of MERSI but the absorption channels of MERSI-II are similar to those of MODIS. Furthermore, the prelaunch
67 and orbital calibration and characterization of MERSI-II were conducted to ensure the quality of its products (Xu et al., 2018).

68 It is necessary to evaluate the satellite-based PWV product ahead of its application in atmospheric science research. The
69 PWV from MODIS has been extensively evaluated by comparing it with the PWV derived from other measurements. The
70 GPS PWV is widely used for the evaluation of PWV derived from MODIS (Liu et al., 2006; Prasad and Singh, 2009; Lu et
71 al., 2011). Ground-based MWR, which can measure integrated water vapor with high temporal resolution and has a reliable
72 measurement under clear sky condition, is also used for the evaluation of MERIS PWV (Li et al., 2003). In addition, the
73 radiosonde PWV, calculated from the integration of specific humidity, has been recognized to be a useful benchmark, being
74 used for the evaluation of the MODIS PWV in China (Liu et al., 2015), the Iberian Peninsula (Sobrino et al., 2014), and Hong
75 Kong (Liu et al., 2013). However, up to now, few studies have focused on the evaluation of the MERSI-II PWV, and the lack
76 of effective assessments greatly limits the application of the MERSI-II PWV product, since the accuracy of the product has
77 not been fully acknowledged.

78 Integrated Global Radiosonde Archive (IGRA) is the greatest and most comprehensive collection dataset of historical and
79 near real-time global quality-assured radiosonde observations. It has been used extensively in a variety of studies, including
80 model verification, atmospheric processes, and climate research. Moreover, the radiosonde PWV is also widely applied in the
81 assessments of measurements from other platforms, especially satellite-derived PWV around the world (Adeyemi and Schulz,
82 2012; Antón et al., 2015; Niilo et al., 2016). Consequently, the IGRA data are selected for the evaluation of the PWV derived
83 from MERSI-II in this study.

84 The purpose of this paper is to evaluate the MERSI-II PWV globally by comparing it with the global IGRA observations.
85 We are seeking to explore the global performance of FY-3D MERSI-II PWV and analyze the influence factors in the evaluation.
86 The structure of this paper is arranged as follows: Data sources and details are discussed in Section 2. Section 3 presents the
87 methodology of the merging procedures applied in the sample selection. The evaluation results of MERSI-II PWV against the
88 PWV from IGRA are presented in Section 4. In the final section, a discussion and conclusion of the aforementioned results
89 are given.

90 **2 Data description**

91 The satellite-based PWV product used in this paper is derived from FY-3D MERSI-II, and the ground-based

92 measurements are the PWV data derived from AERONET and IGRA.

93 2.1 MERSI-II PWV

94 FY-3D, which was successfully launched on 15 November 2017, is the fourth and latest satellite of the second-generation
 95 Chinese polar-orbiting meteorological satellite. It is operated in a sun-synchronous orbit at an average altitude of 830.73 km,
 96 passing over the equator at 13:40 local time (Yang et al., 2019). The MERSI is one of the major instruments carried by FY-3
 97 series satellites, and the MERSI-II onboard FY-3D is an upgraded version of the first-generation instrument. A series of
 98 comprehensive prelaunch calibrations have been operated to ensure the high quality of the products from MERSI-II (Xu et al.,
 99 2018), which is from MERSI and has been significantly improved with high-precision on-board calibration and lunar
 100 calibration capabilities (Wu et al., 2020). Besides, MERSI-II has 25 channels with a spectral coverage from 0.412 μm to 12.0
 101 μm , and the NIR PWV products of FY-3D are retrieved with three water absorption channels (bands 16, 17, and 18) and two
 102 non-absorption channels (bands 15 and 19) in the 0.8–1.3 μm range with a spatial resolution of 1 km \times 1 km at nadir (Wang
 103 et al., 2021). The positions and widths of NIR channels used by MERSI-II and MODIS are given in Table 1. The water vapor
 104 absorption channels of MERSI-II, which is now similar to those of MODIS, are reselected because the three absorption bands
 105 have different sensitivities to various water vapor conditions. Therefore, MERSI-II is more useful in the retrieval of water
 106 vapor under different conditions (dry, medium, and humid).

107 Table 1 Characteristics of NIR channels used in PWV retrievals of MERSI- II and MODIS

MERSI-II				MODIS			
Band No.	Position (nm)	Width (nm)	Window channel	Band No.	Position (nm)	Width (nm)	Window channel
15	865	20	yes	2	865	40	yes
16	905	20	no	17	905	30	no
17	936	20	no	18	936	10	no
18	940	50	no	19	940	50	no
19	1030	20	yes	5	1240	20	yes

108 For the NIR channels, typically with a small aerosol optical thickness that can be ignored, the TOA radiance observed by
 109 a downward-looking satellite sensor can be calculated as the following:

$$110 \quad TOA_{\lambda} = T_{\lambda} \times \rho_{\lambda}, \quad (1)$$

111 where TOA_{λ} , T_{λ} and ρ_{λ} are the apparent reflectance, total atmospheric transmittance and surface bidirectional reflectance
 112 at the channel with a wavelength of λ , respectively. The term $T(\lambda)$ contains information of the total amount of water vapor in
 113 the Sun–surface–sensor path.

114 For most types of land surfaces, a reflectance between 850 and 1250 nm changes approximately linearly with the
 115 wavelength, therefore, the transmittance of the absorption channel will be calculated by a three-channel ratio of the absorption

channel with a combination of two window channels. For the iron-rich soil, the vegetation and snow, although the reflectance does not linearly correlate with the wavelength, reasonable estimates of water vapor transmittances over these surface types can also be given with the three-channel ratio techniques (Gao and Kaufman, 2003).

By using the MODerate resolution atmospheric TRANsmission (MODTRAN), the transmittances of the five MERSI-II channels as a function of the total water vapor amount under six different atmospheric conditions were calculated, according to the six standard atmospheric models defined in MODTRAN4.3. Furthermore, the results are defined as the transmittance–water vapor lookup table. Based on the solar zenith angle and surface temperature, the atmosphere model can be selected from the six standard atmospheric models, and then the combined two-way water vapor content is derived using a table-searching procedure. Note that there are no PWV retrievals in the region with a solar zenith angle above 72° , which means the observation time is close to night, due to the weak energy at the satellite’s entrance. Subsequently, the derived total water vapor amount will be converted to the vertical column water vapor amount based on the solar and observational geometries. The absorption coefficients of atmospheric water vapor are very different over the three absorption channels. As a result, the derived water vapor values from the three channels are different even under the same atmospheric condition. In order to solve this problem, a mean water vapor value is obtained from the water vapor values derived from three absorption channels, by multiplying with the corresponding weight in each channel. A more detailed description of the algorithm of MERSI- II PWV can be found in Wang et al. (2021).

The NIR PWV products derived from MERSI-II have been routinely produced at the National Satellite Meteorological Center, China and can be accessed on the website of <http://satellite.nsmc.org.cn/PortalSite/Data/Satellite.aspx>. The operational NIR PWV products include the Level-2 5-min granule product and Level-3 global daily, 10-day, and monthly mean products. The Level-2 products are generated on a pixel-by-pixel basis (i.e., $1\text{ km} \times 1\text{ km}$) from standard MERSI-II L1B radiance datasets as well as ancillary data from the L1B geolocation and the cloud mask (CLM) product of MERSI- II . The outputs from the Level 2 product include the total weighted column water vapor amount on a pixel-by-pixel basis, independently derived PWV from one of the water vapor absorption channels, and an associated quality assurance parameter that indicates whether the inversion algorithm has a two-channel or three-channel ratio and whether a pixel is clear or cloudy. The Level-2 5-min granule PWV product is evaluated in this study, and the data span is from September 2018 to June 2021 with a spatial resolution of $1\text{ km} \times 1\text{ km}$.

2.2 Radiosonde

The Integrated Global Radiosonde Archive (IGRA), which is a collection of historical and near real-time global radiosonde observations, is archived and distributed by the National Centers for Environmental Information (NCEI), formerly known as the National Climatic Data Center (NCDC), and can be accessed at <ftp://ftp.ncdc.noaa.gov/pub/data/igra>. Version 2 of IGRA (IGRA 2) is used in this study. A total of 33 data sources, including 10 out of 11 source datasets used in IGRA 1,

147 have been integrated into IGRA 2, which was fully operational on August 15, 2016, and has a higher spatial and temporal
148 coverage. Therefore, compared to IGRA 1, the IGRA 2 contains nearly twice as many sounding stations and 30% more
149 soundings. Sounding-derived parameters are recorded according to separated station files and continue to be updated daily,
150 and PWV is one of the derived parameters. PWV will be calculated if the pressure, temperature, and dew point depression are
151 available from the surface to a level of 500 hPa (Durre et al., 2009). The calculation involves the acquirement of specific
152 humidity at each observation level and then the integration of specific humidity between the surface and the level of 500 hPa,
153 so that IGRA-derived PWV is recognized as surface-to-500-hPa PWV. As discussed by Turner et al. (2003), the PWV obtained
154 from radiosonde has an approximate 5% dry bias compared to that derived from the MWR. Therefore, there is an
155 underestimation of PWV evaluation for taking the IGRA-derived PWV as a reference, and the bias found in the tropical area
156 is ~9% (Zhang et al. 2018). Due to the time range of IGRA data, there are only 462 out of 1535 global IGRA stations that can
157 be matched with the FY-3D MERSI-II PWV products.

158 **2.3 AERONET**

159 The federated Aerosol Robotic Network (AERONET) is a network of ground-based Cimel Electronique Sun photometry,
160 which can measure beam irradiance and directional sky radiance routinely during the daytime in clear conditions (Holben et
161 al., 1998). AERONET was established by NASA and PHOTONS (PHOtométrie pour le Traitement Opérationnel de
162 Normalisation Satellitaire), primarily aiming to provide public domain dataset of global aerosol optical and microphysical
163 properties. In addition, based on the measurements at the 940 nm water-vapor channel and the atmospheric window bands
164 centered at 870 nm and 1020 nm, PWV was also calculated (Che et al., 2016). The AERONET version 3 database provides
165 three levels of data: Level 1.0 (unscreened), Level 1.5 (cloud-screened), and Level 2.0 (cloud-screened and quality-assured),
166 and can be accessed at <https://aeronet.gsfc.nasa.gov>. Level 2.0 dataset, which is used in this study, signifies an automatically
167 cloud-cleared, manually quality-controlled dataset with pre- and post-field calibrations applied. All the instruments in the
168 AERONET are annually calibrated with reference to the world standard: the Mauna Loa Observatory (Malderen et al., 2014).
169 Thus, the measuring accuracies of different AERONET stations are accurate and consistent (Liu et al., 2013). As discussed by
170 Pérez-Ramírez et al. (2014), PWV obtained from AERONET has a dry bias of approximately 0.16 cm against the radiosonde
171 PWV and it is reasonable for meteorological studies.

172 **3 Methodology**

173 **3.1 Statistical indicators**

174 The common statistical indicators, such as the mean bias (MB, perfect value = 0), the mean relative bias (MRB, perfect

value = 0), correlation coefficient (CC, perfect value = 1) and the root mean squared error (RMSE, perfect value = 0), are used to evaluate the precision of the retrieved PWV from MERSI- II . All calculations of indicators are presented as follows:

$$MB = \frac{1}{N} \sum_{i=1}^N (PWV_{si} - PWV_{gi}) , \quad (2)$$

$$MRB = \frac{1}{N} \sum_{i=1}^N \left(\frac{PWV_{si} - PWV_{gi}}{PWV_{gi}} \right) \times 100\% , \quad (3)$$

$$CC = \frac{\sum_{i=1}^N (PWV_{si} - \overline{PWV_{si}})(PWV_{gi} - \overline{PWV_{gi}})}{\sqrt{\sum_{i=1}^N (PWV_{si} - \overline{PWV_{si}})^2 \sum_{i=1}^N (PWV_{gi} - \overline{PWV_{gi}})^2}} , \quad (4)$$

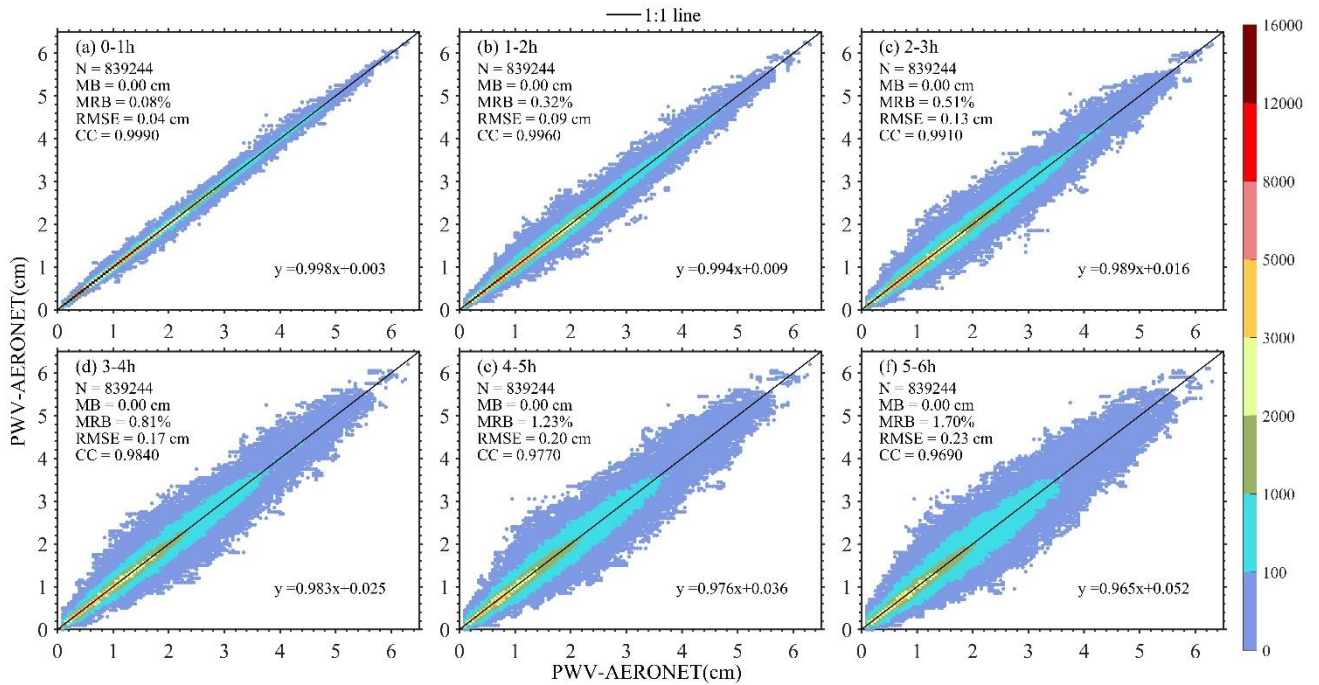
$$RMSE = \sqrt{\frac{1}{N} \sum_{i=1}^N (PWV_{si} - PWV_{gi})^2} \quad (5)$$

where PWV_s is the MERSI- II PWV product, PWV_g is the IGRA PWV product, and N is the total number of match-up.

3.2 Collocation strategy

As we have mentioned above, FY-3D is operated in a Sun-synchronous orbit with an equator crossing time at 13:40 local time. However, the radiosonde is released at 00:00 UTC and 12:00 UTC and there is a significant temporal discrepancy between satellite and radiosonde at most sites. Furthermore, the distribution of radiosonde site is sparse over the globe. For the evaluation of PWV from global reanalysis models with a temporal resolution of 6 h, temporal window of ± 3 h and distance of ± 50 km is employed in the comparison with PWV from Maritime Aerosol Network (Pérez-Ramírez et al., 2019).

In order to determine the temporal collocation window that can adequately match the satellite observations with the ground-based measurements, the consistencies between the existing AERONET PWV and the temporal averaged AERONET PWV in various temporal discrepancy intervals from 1 h to 6 h with a step of 1 h, that is, 0–1 h, 1–2 h, etc., are analyzed respectively. In processing, only the existing AERONET PWV, which has the matching averaged AERONET PWV in each temporal discrepancy interval, is selected for the determination of the temporal collocation window. Therefore, there is the same number of collocations for all the temporal discrepancy intervals. The results are presented in Figure 1, and as evidenced, there is a good consistency in all situations with the CC larger than 0.969 and the slope larger than 0.965. Although MRB and RMSE become larger with the increasing temporal interval, their values are less than 1.7% and 0.23 cm, respectively. Moreover, it can be observed that the MB values of all comparisons are 0.00 cm, which suggest that the biases are distributed equally around zero. Therefore, we conclude that the temporal collocation window for PWV evaluation can be set to 6 h.



198

199 Figure 1 Scatter plots of PWV derived from AERONET in different temporal discrepancy intervals and (a)–(f) present the
 200 temporal discrepancy of 0–1 h, 1–2 h, 2–3 h, 3–4 h, 4–5 h and 5–6 h, respectively. The solid line represents the 1:1 line. The
 201 colorbar depicts the number density of match-ups for each bin of PWV in a 0.01 cm×0.01 cm grid.

202 For the MERSI- II , the spatial resolution at nadir is 1 km × 1 km for NIR bands, which are used for the retrieval of PWV.
 203 It is not perfectly justifiable that the PWV in an image pixel represents the surrounding averaged PWV (Ichoku et al., 2002),
 204 and during the ascending of balloon, its lateral drift should also be considered. Therefore, the spatial averaged PWV within a
 205 box of 9×9 pixels was calculated. Furthermore, only when all pixels within the box are confidently proved to be clear by the
 206 MERSI- II CLM product, the pixel is marked as reliable and the PWV of the central pixel is replaced by the spatially averaged
 207 PWV value. Otherwise, the pixel is marked as unreliable and will not be selected for the comparison. Unfortunately, there is
 208 no cloud measurement in the radiosonde observation, so the cloud detection method with the relative humidity threshold of
 209 sounding is employed here (Zhang, 2010), and then the cloudless radiosonde PWV dataset is established.

210 In this study, the threshold of the horizontal distance between an IGRA station and the footprint of MERSI-II is set to be
 211 50 km (Qin et al., 2012; Pérez-Ramírez et al., 2019). In processing, all the reliable PWV retrievals derived from MERSI- II
 212 within ± 6 h of the radiosonde release time are collected and only the spatial closest PWV retrieval within a 50 km distance
 213 from the IGRA site is selected and matched with the IGRA-derived PWV. Figure 2 illustrates the available sample numbers
 214 of radiosonde sites over the globe from 2018–2021, with a total of 462 sites. The sample numbers of all sites vary from 15 to
 215 418, and observations are concentrated in the Northern Hemisphere. Around the equator, few samples are obtained due to the

high occurrence frequency of clouds and precipitation. Most frequently sampled places are China, Europe, and North America, where IGRA sites are densely distributed, while there are few match-ups in Africa since radiosonde stations associated with IGRA in this region are sparse (Durre et al., 2018).

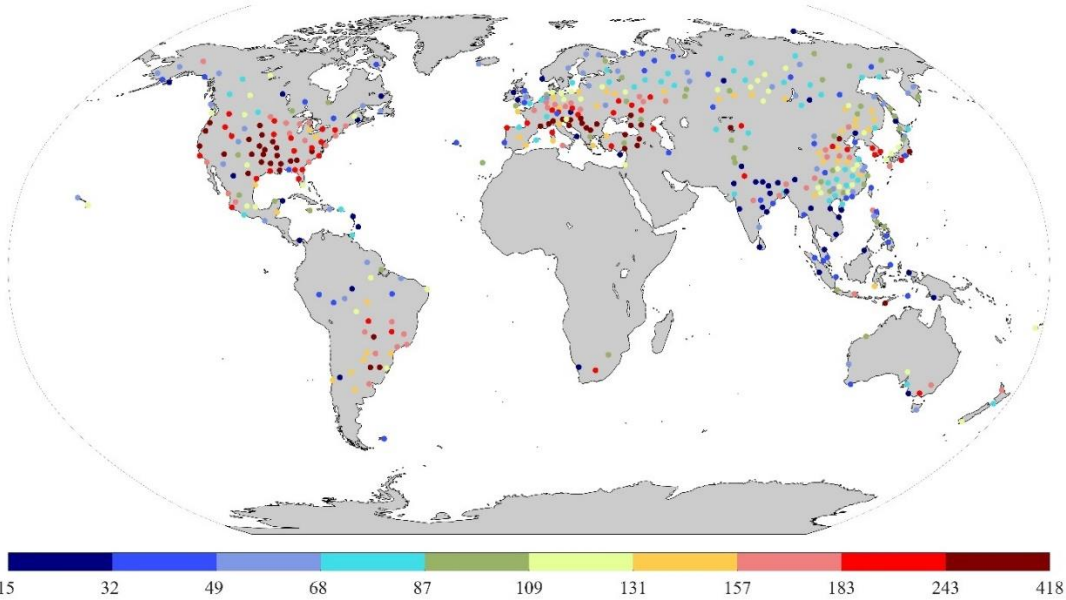
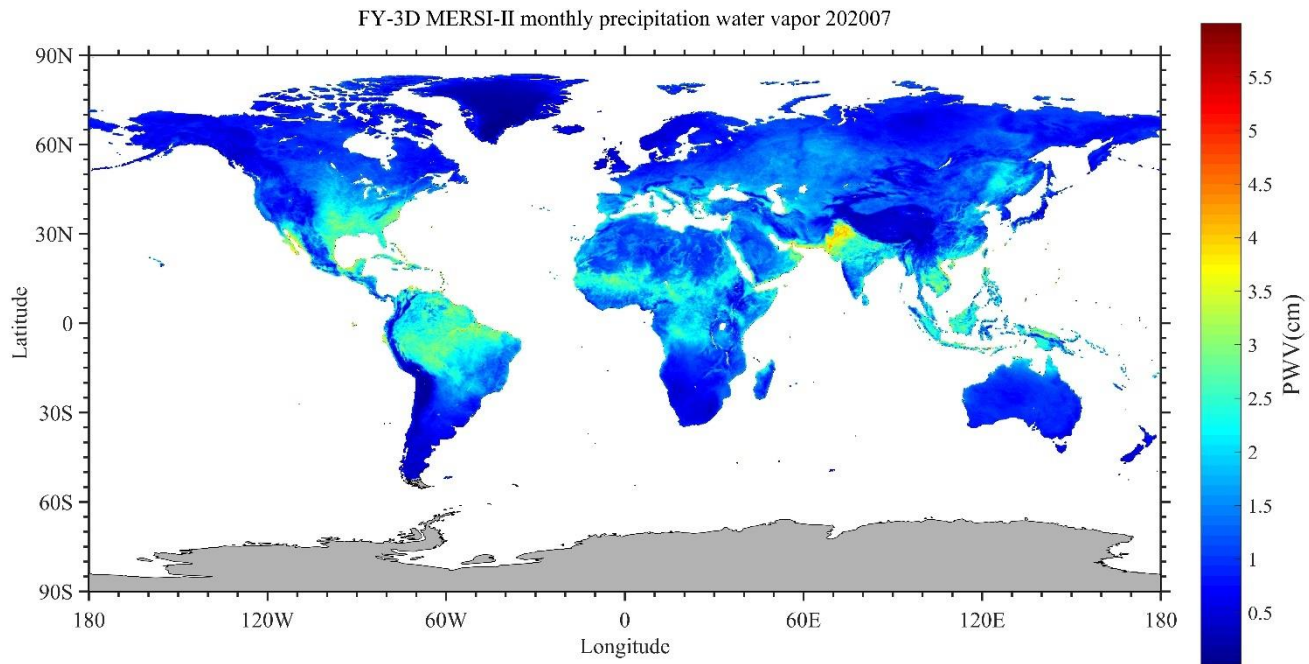


Figure 2 Number of matchups between MERSI-II and IGRA PWV observations for each site from 2018–2021.

4 Results and Discussion

4.1 Global evaluation of PWV derived from MERSI- II

Figure 3 illustrates the global monthly averaged PWV obtained from the MERSI- II for the month of July in 2020. In general, the averaged PWV derived from MERSI- II shows a decreasing distribution of PWV with increasing latitude, and large PWV values are mostly found in the tropics but rare in high latitudes. High PWV values (> 3.0 cm) are mostly detected in the Amazon rainforest of South America, West and South Asia, southeastern China, Southeast Asian islands, and central Africa. The significantly high PWV center in West Asia is mainly contributed by the Indian moon during the summer season. The PWV contents over the Qinghai–Tibet Plateau and Greenland are small because of the high altitude and high latitude, respectively. Furthermore, due to the winter season of July in the Southern Hemisphere, small PWV contents are also presented over the southern parts of South America and Africa, as well as Australia.

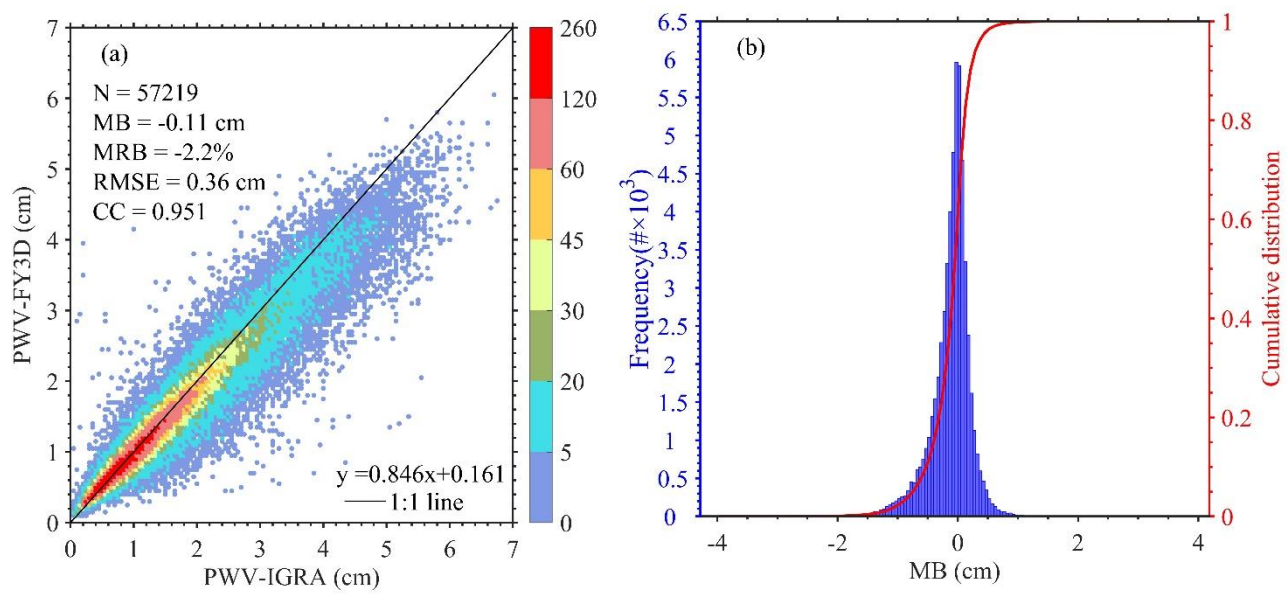


231

232 Figure 3 Global averaged Level-3 NIR precipitable water vapor (PWV) image derived from FY3D MERSI-II in July 2020 .

233 Figure 4a shows the scatter plot of PWV derived from MERSI- II against IGRA observations. There are 57,219 match-
 234 ups in total and the MERSI- II (IGRA) PWV ranges from 0.11(0.05) cm to 6.07 (6.78) cm, with a high number density between
 235 0.20 cm and 2.00 cm. Moreover, it is found that the MERSI- II and IGRA PWV measurements are well correlated with CC of
 236 0.951, while the retrieved PWV from MERSI- II is slightly underestimated, with an MB of -0.11 cm and an MRB of -2.2%.
 237 Furthermore, the RMSE is 0.36 cm and the statistical biases are slightly larger than those from the evaluation of MODIS over
 238 globe by comparing with the observations of AERONET (Martins et al., 2019). It is considered that the satellite has a larger
 239 temporal discrepancy with radiosonde than AERONET, which has a high temporal resolution of about 1 min, and from the
 240 discussion in section 3.2, a large temporal discrepancy will cause an increasing bias in the evaluation of the PWV product.
 241 Figure 4b reveals the distribution of MB between FY-3D MERSI-II and IGRA with a bin width of 0.05 cm, and notably, the
 242 MB is concentrated around zero and there is a small flattening towards negative values. Moreover, there are 20.8% of all points
 243 within the interval from -0.05 cm to 0.05 cm, and the standard deviation (STD) of MB is 0.34 cm. It can be concluded that
 244 there is high accuracy for the MERSI- II PWV product, as evidenced by the low MB and STD which are similar to those in
 245 the evaluation of ground-based GPS PWV against radiosonde PWV (Wang et al., 2007). Although the MB is mainly distributed
 246 between -1.00 cm and 0.50 cm, it is observed that there are also some points with a large MB value. As presented in figure 4b,
 247 the large MB is mostly with a negative value, and this is mainly due to the different situations observed by the radiosonde and

248 satellite because of the radiosonde drift and the large temporal discrepancy between MERSI- II and IGRA observations. Due
 249 to the lack of cloud measurement in the radiosonde observation, the PWV from IGRA possibly contains the point in cloudy
 250 conditions, which is proved to have a larger water content than clear conditions (Zhang et al., 2015). For most large positive
 251 MRB, there is a large temporal discrepancy of more than 4 h, and this is recognized as the primary reason for the high positive
 252 MRB.



254 Figure 4 (a) Total density scatterplot of the PWV derived from MERSI- II against that of IGRA for each bin of PWV in a 0.05
 255 cm×0.05 cm grid. The solid line represents the 1:1line. (b) Frequency histogram of MB between MERSI- II and IGRA PWV
 256 superimposed on a cumulative distribution curve.

257 **4.2 Evaluation of MERSI- II PWV product in different locations**

258 Figure 5 shows the geographical distributions of PWV comparison statistics of 462 sites between MERSI- II and IGRA
 259 over the globe. In order to equally present the statistical indicators, all sites are separated into approximately ten equal parts,
 260 that is, the site number of each part is ~43. Consequently, the steps of comparison statistics are not equidistant in the
 261 presentation. As we can see from the MB distribution in Figure 5a, the MB mostly presents a low value between -0.41 cm and
 262 0.05 cm. About 80% of all sites have negative MB values, and this indicates that PWVs derived from MERSI- II are primarily
 263 underestimated compared with IGRA PWV values. Most sites with an MB value larger than -0.41 cm are distributed in the
 264 west and south of Asia, with a large mean PWV content but a small number of match-ups. Furthermore, attributed to the
 265 monsoon climate, there is a large seasonal variation over this region, particularly in the south foothill of the Himalayas (Chen

266 and Liu, 2016). Those sites with overestimated PWV values of MERSI- II are mostly distributed in the surrounding areas of
267 the Black Sea and central South America, and most of them have MB values larger than 0.05 cm. It is also found in the
268 evaluation of the PWV product derived from MODIS onboard Terra that the MB of MERSI- II is slightly smaller (Martins et
269 al., 2019). In general, the distribution of the MRB (Figure 5b) is similar to that of the MB at most sites. However, there are
270 two areas that have slight discrepancies between them. One area is in eastern Russia and northeastern China, where there are
271 some sites with a large MRB value above 3.3%, although with a small MB value ranging from -0.10 cm to 0.05 cm. As we
272 can see from figure 3, there is a low averaged PWV value in this region, and this is the dominant reason for the great MRB
273 values but with small MB values over this area. Another area is central South America, where the sites have large MB values
274 and comparatively low MRB values, and this is because of the large mean PWV values in this region. The larger evaluation
275 bias of PWV derived from MODIS and reanalysis products has also been found in the middle of South America, with most
276 sites having the MB and RMSE both larger than 0.40 cm (Lu, 2019; Wang et al., 2020). Figure 4c depicts the distributions of
277 RMSE for all sites and most sites have a small RMSE below 0.48 cm. The large RMSE values are primarily found at low
278 latitudes, mostly in South and Southeast Asia. However, in the east of Europe, there are small RMSE with values below 0.21
279 cm at most sites. In general, there is a good agreement between MERSI- II and IGRA PWV at most sites with the CC value
280 above 0.873. The highly correlated sites are mainly distributed around the east of Europe and have CC values larger than 0.958,
281 while low CC values smaller than 0.814 are predominantly concentrated around the equator. There are large biases but small
282 CC values over the equator, and that is possibly due to the following: 1) large residual IGRA PWV above 500 hPa (Boukabara
283 et al., 2010); 2) high content and variation of PWV (Chen and Liu, 2016); 3) the covered surface with the reflectance does not
284 linearly correlate with the wavelength (Gao and Kaufman, 2003); 4) a small number of samples. In addition, the temporal
285 discrepancy can also lead to bias because the discrepancy in the equatorial region is slightly larger than in other regions overall.
286 As discussed by Alraddawi et al (2018), for MODIS PWV, there are also noteworthy latitudinal decreases for MB, MRB and
287 RMSE.

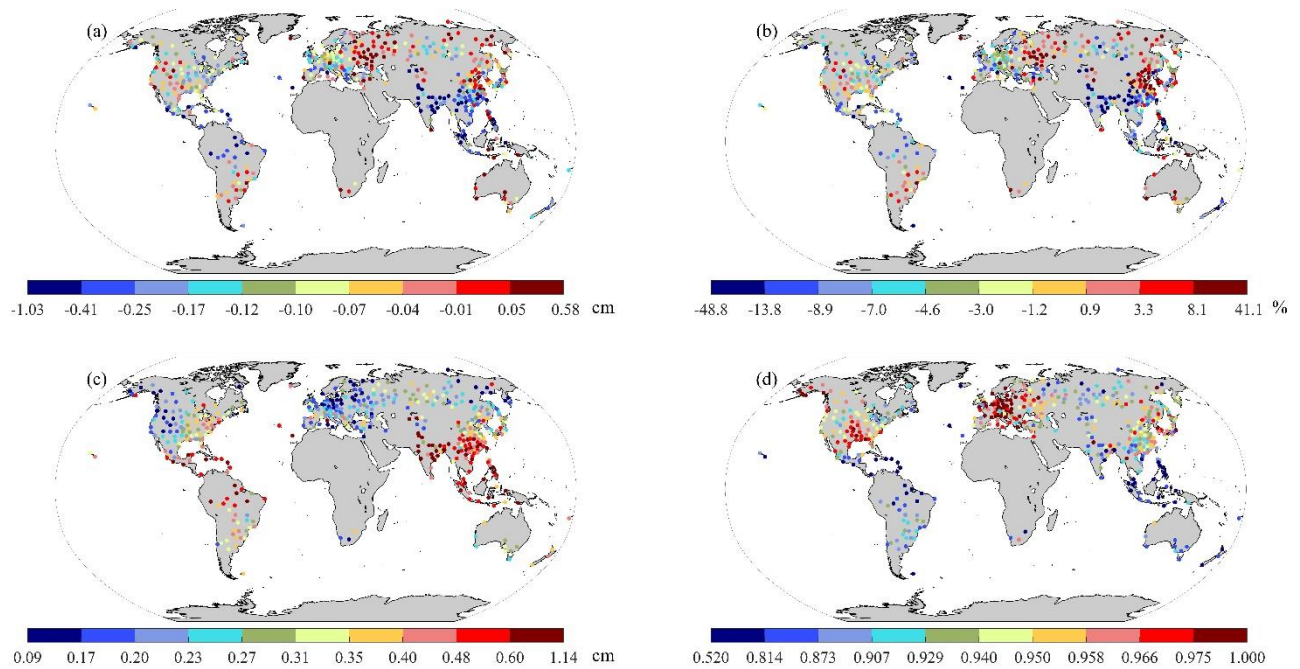


Figure 5 The geographical distributions of PWV comparison statistics between MERSI- II and IGRA. (a) MB; (b) MRB; (c) RMSE; (d) CC.

4.3 The annual performance of MERSI- II PWV product

As we mentioned above, PWV presents a notable temporal variation. Therefore, the annual performance of the MERSI- II PWV product by season was evaluated and the results are given in Table 2. It is noted that the number of samples in each season is significantly different.

Table 2 Seasonal statistics of comparison between PWVs derived from MERSI- II and IGRA in the Northern (Southern) Hemisphere

Season	N	Slope	MB (cm)	MRB (%)	RMSE (cm)	CC
MAM	11866(1232)	0.833(0.859)	-0.09(-0.10)	-1.8(-1.4)	0.31(0.39)	0.954(0.953)
JJA	15935(2187)	0.807(0.873)	-0.18(-0.05)	-5.3(1.7)	0.41(0.34)	0.931(0.953)
SON	16196(2176)	0.836(0.858)	-0.11(-0.06)	-2.5(0.3)	0.34(0.41)	0.945(0.933)
DJF	6558(1069)	0.852(0.799)	-0.05(-0.17)	3.8(-3.9)	0.31(0.49)	0.944(0.921)

The number of match-ups ranges from 6558 (1069) to 16196 (2187) in the Northern (Southern) Hemisphere for all seasons. In all seasons, the slope values are all less than 0.873, which is the fit-slope in winter in the Southern Hemisphere. The MERSI- II PWV is underestimated for all seasons, and the MB is less than -0.18 cm. The MB is obviously large in the warm season, and it is more significant during the summer. With abundant water vapor in summer, clouds easily form, however, thin clouds

are difficult to be measured by satellite due to their low optical depth (Solbrig, 2009; Naumann and Kiemle, 2020). Therefore, the higher underestimation of PWV in summer is probably triggered by the weakened or covered radiation signal under the thin cloud. For MRB, the variation is within a large range, and the largest MRB is in summer over both the Northern and Southern Hemisphere, with values of -5.3% and -3.9%, respectively. For the largest MRB during winter in the Northern Hemisphere, this might be related to the points with a small PWV value but a high positive MB, because we firstly calculate the MRB for each match-up and then average all MRB values in seasons. In addition, MRB is mostly negative during the warm season, but positive in the cold season. The RMSE in the Northern Hemisphere is slightly smaller than that in the Southern Hemisphere, where the greatest RMSE value is 0.49 cm in summer. There is a large oceanic coverage in the Southern Hemisphere, with a larger mean PWV than that in the Northern Hemisphere (Chen and Liu, 2016). Thus, this is a possible reason accounting for large RMSE in the Southern Hemisphere, considering the increasing bias of the remote sensing PWV with the larger PWV value. Moreover, there is an improved correlation between PWV derived from MERSI-II and IGRA, and all CC values are larger than 0.921.

4.4 Influencing factors on evaluation

As mentioned above, there is a higher bias with the larger PWV value, and this is found in the evaluation of MODIS PWV product (Martins et al., 2019). Furthermore, the impact of the spatial distance between the footprint of the satellite and the IGRA station on the evaluation of PWV is also considered in the validation of HY-2A CMR PWV (Wu et al., 2020b). In this section, influencing factors such as the value of IGRA PWV and the spatial distance between the footprint of the satellite and the IGRA station, are all explored in order to quantify their effects on the evaluation of MERSI- II PWV. Table 3 illustrates the evaluation results of the MERSI-II PWV in different intervals of IGRA PWV and spatial distance. All metrics are calculated using all match-ups.

Table 3 Statistics of the global evaluation of MERSI-II PWV in different PWV and distance ranges.

	Intervals	N	Slope	MB (cm)	MRB (%)	RMSE (cm)	CC
IGRA PWV (cm)	(0, 1]	15528	0.869	0.04	9.0	0.17	0.754
	(1, 2]	21698	0.878	-0.06	-3.7	0.26	0.709
	(2, 3]	11831	0.842	-0.19	-7.8	0.41	0.556
	(3, 4]	5493	0.867	-0.35	-10.1	0.57	0.483
	(4, 5]	2122	0.664	-0.55	-12.3	0.72	0.358
	>5	547	0.636	-0.94	-17.4	1.10	0.347
Spatial distance (km)	(0, 5]	31216	0.860	-0.08	-0.6	0.33	0.952
	(5, 10]	19972	0.844	-0.14	-3.4	0.38	0.953
	(10, 20]	4800	0.813	-0.19	-6.1	0.42	0.951
	>20	1231	0.792	-0.20	-5.9	0.47	0.933

322 Firstly, the IGRA PWV is binned and compared with the MERSI-II PWV. Most match-ups are located at the IGRA PWV
323 interval ranging from 1.0 to 2.0 cm, and there are not many samples above 5.0 cm. The MB and RMSE gradually increase
324 with the increasing content of PWV, from 0.04 cm and 0.17 cm to -0.94 cm and 1.10 cm, respectively. Moreover, the fit-slope
325 value is generally decreasing with the increasing content of PWV, and it can be concluded that there is an obvious
326 underestimation when the PWV is larger than 5.0 cm. This result is similar to the conclusion drawn by Martins et al. (2019) in
327 the evaluation of the PWV from MODIS, however, the slope is smaller. There is a good agreement between the IGRA PWV
328 and MERSI-II PWV for dry conditions (<1.0 cm), with the highest CC value of 0.754. However, a slightly large discrepancy
329 is observed in wet conditions (> 5.0 cm). For MRB, there is a positive value of 9.0% in the 0.0–1.0 cm interval, and this is also
330 caused by the small PWV value. In contrast, all MRB is negative and the value of MRB increases with the content of PWV
331 above 1.0 cm.

332 The results of the MERSI-II PWV and IGRA PWV comparison in different distance intervals are also presented in Table
333 3. Most points are located within the 0–5 km distance interval, and the number of points is 31,216 out of all 57,219 points. The
334 MB increases with the extension of the distance between the IGRA station and the footprint of MERSI-II, and the largest MB
335 is -0.20 cm when the distance is larger than 20 km. For the MRB, a more obvious difference is present within the 0–20 km
336 distance range, as the value increases from -0.6% to -6.1% with the increasing distance. However, there is a slightly smaller
337 MRB when the distance is larger than 20 km, and this probably has a relationship with the small number of samples. The
338 RMSE has a value ranging from 0.33 cm to 0.47 cm and becomes larger with the increasing distance. The large RMSE in the
339 distance above 20 km is mainly caused by the obvious underestimation of MERSI-II PWV at some points. Overall, a good
340 correlation exists between MERSI-II PWV and IGRA PWV with the CC value larger than 0.933.

341 **5 Summary and Conclusions**

342 In this paper, we evaluated the global PWV product derived from FY-3D/MERSI-II by comparing with the PWV from
343 462 IGRA stations, with 57,219 match-ups during the period from September 2018 to June 2021. The monthly averaged PWV
344 derived from MERSI-II shows a distribution of decreasing values with an increasing latitude.

345 Overall, PWVs derived from MERSI-II and IGRA are in good agreement with the CC value of 0.951. However, there is
346 a slight underestimation for the FY-3D/MERSI-II PWV, and the values of MB and MRB are -0.11 cm and -2.2%, respectively,
347 while the RMSE is 0.36 cm. The histogram of MB indicates that MB value approaches zero and mostly distributes between -
348 1.00 cm and 0.50 cm with a left-skewed distribution pattern.

349 For all sites, the MB value is low and most sites have a value between -0.41 cm and 0.05 cm. In the west and south of
350 Asia, the MERSI-II PWV is obviously underestimated with an MB value larger than -0.41 cm. However, the overestimated
351 PWV are mostly distributed in the surrounding areas of the Black Sea and central South America. Large MRB values are

352 mostly located in eastern Russia, northeastern China, and central South America. Most sites have a small RMSE below 0.48
353 cm, and CC values above 0.873. Lastly, it is observed that there are large MB and RMSE values while there are small CC
354 values around the equator, especially in South and Southeast Asia.

355 The MERSI- II PWV is in good agreement with the PWV obtained from IGRA with all CC values larger than 0.921.
356 There is a slight underestimation of MERSI- II PWV for all seasons with an MB value below -0.18 cm, and it is significant in
357 the summer. In addition, the MRB and RMSE also have the largest magnitude in summer. The underestimation of PWV in
358 summer is probably due to the presence of thin clouds, which weaken the radiation signal observed by the satellite. We found
359 the MRB with a positive value in the winter, and this is mainly due to the low PWV then. For RMSE, there is a larger value in
360 the Southern Hemisphere and the greatest RMSE value is 0.49 cm in summer.

361 In addition, the influencing factors on the evaluation are also discussed. First of all, there is an obvious effect of binned
362 IGRA PWV on the evaluation, and in general, the MB and RMSE are both increasing with the IGRA PWV. In the dry condition
363 (<1.0 cm), there is a positive MRB value of 9.0%, and this is also mainly due to the low PWV value. Nevertheless, the MRB
364 is all negative and increases with an IGRA PWV above 2.0 cm. Subsequently, the evaluations within different distance intervals
365 are presented in order to reveal the effect of distance between the footprint of the satellite and the IGRA site location. The MB
366 varies positively with the increasing distance, and the largest MB is -0.20 cm within the distance above 20 km. The MRB
367 increases from -0.6% to -6.1% with the distance increases from 0 to 20 km. The RMSE also increases with the distance
368 increased and the large RMSE is mainly caused by the obvious underestimation of MERSI-II PWV at some points with the
369 spatial distance larger than 20 km.

370 The global evaluation of the MERSI- II PWV product can explore a wide variety of applications of this product, and the
371 analysis of the influencing factors on the evaluation can be helpful for improving the PWV retrieval algorithm. Although we
372 have partially explained the underestimation of the PWV from MERSI- II , other influencing factors, such as the solar zenith
373 angle, the precision of the transmittance calculation and the uncertainty of the radiation signals should be studied in the future.
374 Furthermore, how to quantitate the influence of aerosols (e.g., dust, haze) and thin cirrus clouds on the PWV retrieval is also
375 a key problem that should be explored in the application of the PWV product.

376 **Data availability**

377 The MERSI-II PWV product is available from <http://satellite.nsmc.org.cn/PortalSite/Data/Satellite.aspx>, the IGRA data is
378 available from <ftp://ftp.ncdc.noaa.gov/pub/data/igra>, and the global AERONET data are provided at
379 <https://aeronet.gsfc.nasa.gov>. The altitude data set is provided by Geospatial Data Cloud site, Computer Network Information
380 Center, Chinese Academy of Sciences at <http://www.gscloud.cn>. The processed data are available from Zenodo
381 (<https://doi.org/10.5281/zenodo.5563205>).

382 **Author contributions**

383 Conceptualization, ZWG and WL; data curation, WL, YY and HQX; formal analysis, ZWG, YY and XGR; writing-original
384 draft preparation, ZWG; writing-review and editing, ZWG and WL; supervision, XGR and HXQ; funding acquisition, XGR
385 and CCG. All authors have reviewed and agreed on the final version of the manuscript.

386 **Competing interests**

387 The authors declare that they have no conflict of interest.

388 **Acknowledgments**

389 This work is supported by The Second Tibetan Plateau Scientific Expedition and Research (STEP) program (Grant No.
390 2019QZKK0105); National Natural Science Foundation of China (NSFC) under Grant No. 41705019 and 41620104009; the
391 Hubei Meteorological Bureau project under Grant No. 2018Q04; and NSFC under Grant No. 91637211. We appreciate the
392 National Satellite Metrological Center of China Meteorological Administration (CMA) for providing the MERSI-II PWV
393 product, the National Climatic Data Center (NCDC) for providing IGRA data, and the principal investigators and their staff
394 for establishing and maintaining the AERONET sites used in this study. The altitude data set is provided by Geospatial Data
395 Cloud site, Computer Network Information Center, Chinese Academy of Sciences.

396 **References**

397 Adeyemi, B. and Schulz, J.: Analysis of water vapor over nigeria using radiosonde and satellite data, *J. Appl. Meteor. Climatol*,
398 51, 1855-1866, <https://doi.org/10.1175/JAMC-D-11-0119.1>, 2012.

399 Alexandrov, M. D., Schmid, B., Turner, D. D., Cairns, B., Oinas, V., Lacis, A.A., Gutman S. I., Westwater, E. R. Smirnov,
400 A., and Eilers J.: Columnar water vapor retrievals from multifilter rotating shadow band radiometer data, *J. Geophys. Res.*
401 *Atmos.*, 114, D02306, <https://doi.org/10.1029/2008JD010543>, 2009.

402 Alraddawi, D., Sarkissian, A., Keckhut, P., Bock, O., Noël, S., and Bekki, S.: Comparison of total water vapour content in the
403 Arctic derived from GNSS, AIRS, MODIS and SCIAMACHY, *Atmos. Meas. Tech.*, 11(5), 2949-2965,
404 <https://doi.org/10.5194/amt-11-2949-2018>, 2018.

405 Antón, M., Loyola, D., Román, R., and Vömel, H.: Validation of GOME-2/MetOp-A total water vapour column using
406 reference radiosonde data from the GRUAN network, *Atmos. Meas. Tech.*, 8, 1135-1145, [https://doi.org/10.5194/amt-8-](https://doi.org/10.5194/amt-8-1135-2015)
407 1135-2015, 2015.

408 Bennartz, R., and Fischer, J.: Retrieval of columnar water vapour over land from back-scattered solar radiation using the

Medium Resolution Imaging Spectrometer (MERIS), *Remote Sens. Environ.*, 78(3), 274-283,
[https://doi.org/10.1016/S0034-4257\(01\)00218-8](https://doi.org/10.1016/S0034-4257(01)00218-8), 2001.

Bevis, M., Businger, S., Herring, T. A., Rocken, C., Anthes, R. A., and Ware, R. H.: GPS meteorology: Remote sensing of
atmospheric water vapor using the Global Positioning System, *J. Geophys. Res. Atmos.*, 97(D14), 15787-15801,
<https://doi.org/10.1029/92JD01517>, 1992.

Boukabara, S., Garrett, K., and Chen, W.: Global Coverage of Total Precipitable Water Using a Microwave Variational
Algorithm, *IEEE T. Geosci. Remote*, 48, 3608-3621, <https://doi.org/10.1109/TGRS.2010.2048035>, 2010.

Che, H. Z., Gui, K., Chen, Q. L., Zheng, Y., Yu, J., Sun, T. Z., Zhang, X. Y., and Shi, G. Y.: Calibration of the 936 nm water-
vapor channel for the China aerosol remote sensing NETwork (CARSNET) and the effect of the retrieval water-vapor on
aerosol optical property over Beijing, China, *Atmos. Pollut. Res.*, 7(5), 743-753,
<https://doi.org/10.1016/j.apr.2016.04.003>, 2016.

Chen, B. and Liu, Z.: Global water vapor variability and trend from the latest 36 year (1979 to 2014) data of ECMWF and
NCEP reanalyses, radiosonde, GPS, and microwave satellite, *J. Geophys. Res. Atmos.*, 121, 11442-11462,
<https://doi.org/10.1002/2016JD024917>, 2016.

Dessler, A.E. and Wong, S.: Estimates of the water vapor climate feedback during El Niño–Southern Oscillation, *J. Climate*,
22(23), 6404-6412, <https://doi.org/10.1175/2009JCLI3052.1>, 2009.

Durre, I., Williams Jr., C. N., Yin, X. G., and Vose, R. S.: Radiosonde-based trends in precipitable water over the Northern
Hemisphere: An update, *J. Geophys. Res. Atmos.*, 114, D05112, <https://doi.org/10.1029/2008JD010989>, 2009.

Durre, I., Yin, X., Vose, R. S., Applequist, S., and Arnfield, J.: Enhancing the Data Coverage in the Integrated Global
Radiosonde Archive, *J. Atmos. Ocean. Tech.*, 35(9), 1753-1770, <https://doi.org/10.1175/JTECH-D-17-0223.1>, 2018.

Gao, B. C. and Kaufman, Y. J.: Water vapor retrievals using Moderate Resolution Imaging Spectroradiometer (MODIS) near-
infrared channels, *J. Geophys. Res. Atmos.*, 108, D13, <https://doi.org/10.1029/2002JD003023>, 2003.

Held, I. M. and Soden, B. J.: Water vapor feedback and global warming, *Annu. Rev. Energy Environ.*, 25, 441-475,
<https://doi.org/10.1146/annurev.energy.25.1.441>, 2000.

Holben, B. N., Eck, T. F., Slutsker, I., Tanré, D., Buis, J. P., Setzer, A., Vermote, E., Reagan, J.A., Kaufman, Y.J., Nakajima,
T., Lavenue, F., Jankowiak, I., and Smirnov, A.: AERONET—A federated instrument network and data archive for aerosol
characterization, *Remote Sens. Environ.*, 66(1), 1-16, [https://doi.org/10.1016/S0034-4257\(98\)00031-5](https://doi.org/10.1016/S0034-4257(98)00031-5), 1998.

Kiehl, J. T. and Trenberth, K. E.: Earth's annual global mean energy budget, *B. Am. Meteorol. Soc.*, 78, 197-208,
[https://doi.org/10.1175/1520-0477\(1997\)078%3C0197:EAGMEB%3E2.0.CO;2](https://doi.org/10.1175/1520-0477(1997)078%3C0197:EAGMEB%3E2.0.CO;2), 1997.

Li, Z. H., Muller, J. P., Cross, P., Albert, P., Hewison, T., Watson, R., Fischer, J., and Bennartz, R.: Validation of MERIS near
IR water vapour retrievals using MWR and GPS measurements, MERIS user workshop, ESA ESRI, Frascati, Italy, 10-
13 Nov 2003, 2003.

Liu, H. L., Tang, S. H., Zhang, S. L., and Hu, J. Y.: Evaluation of MODIS water vapour products over China using radiosonde
data, *Int. J. Remote Sens.*, 36(2), 680-690, <https://doi.org/10.1080/01431161.2014.999884>, 2015.

Liu, J. M., Liang, H., Sun, Z. A., and Zhou, X. J.: Validation of the Moderate-Resolution Imaging Spectroradiometer
precipitable water vapor product using measurements from GPS on the Tibetan Plateau, *J. Geophys. Res. Atmos.*, 111,

445 D14103, <https://doi.org/10.1029/2005JD007028>, 2006.

446 Liu, Z. Z., Wong, M. S., Nichola, J. and Chan, P. W.: A multi-sensor study of water vapour from radiosonde, MODIS and
 447 AERONET: a case study of Hong Kong, *Int. J. Climatol.*, 33, 109-120, <https://doi.org/10.1002/joc.3412>, 2013.

448 Lu, N.: Biases and abrupt shifts of monthly precipitable water from Terra MODIS, *Remote Sens.*, 11(11), 1315.
 449 <https://doi.org/10.3390/rs11111315>, 2019.

450 Lu, N., Qin, J., Yang, K., Gao, Y., Xu, X. D., and Koike, T.: On the use of GPS measurements for Moderate Resolution
 451 Imaging Spectrometer precipitable water vapor evaluation over southern Tibet, *J. Geophys. Res. Atmos.*, 116, D23117,
 452 <https://doi.org/10.1029/2011JD016160>, 2011.

453 Malderen, R. V., Brenot, H., Pottiaux, E., Beirle, S., Hermans, C., Mazière, M. D., Wagner, T., Backer, H. D., and Bruyninx,
 454 C.: A multi-site intercomparison of integrated water vapour observations for climate change analysis, *Atmos. Meas. Tech.*,
 455 7, 2487-2512, <https://doi.org/10.5194/amt-7-2487-2014>, 2014.

456 Martins, V. S., Lyapustin A., Wang, Y. J., Giles, D. M., Smirnov, A., Slutsker, I., and Korkin S. Global validation of columnar
 457 water vapor derived from EOS MODIS-MAIAC algorithm against the ground-based AERONET observations, *Atmos.*
 458 *Res.*, 225, 181-192, <https://doi.org/10.1016/j.atmosres.2019.04.005>, 2019.

459 Meng, X. C., Cheng, J. and Liang, S. L.: Estimating land surface temperature from Feng Yun-3C/MERSI data using a new
 460 land surface emissivity scheme, *Remote Sens.*, 9(12), 1247, <https://doi.org/10.3390/rs9121247>, 2017.

461 Naumann, A. K. and Kiemle, C.: The vertical structure and spatial variability of lower-tropospheric water vapor and clouds in
 462 the trades, *Atmos. Chem. Phys.*, 20, 6129-6145, <https://doi.org/10.5194/acp-20-6129-2020>, 2020.

463 Niilo, K., Jukka, K., Viktoria, S., Johanna, T., Margherita, G., and Pieter, V.: Validation of GOME-2/Metop total column water
 464 vapour with ground-based and in situ measurements, *Atmos. Meas. Tech.*, 9, 1533-1544, [https://doi.org/10.5194/amt-9-](https://doi.org/10.5194/amt-9-1533-2016)
 465 1533-2016, 2016.

466 Pérez-Ramírez, D., Whiteman, D. N., Smirnov, A., Lyamani, H., Holben, B. N., Pinker, R., Andrade, M., and Alados-
 467 Arboledas, L.: Evaluation of AERONET precipitable water vapor versus microwave radiometry, GPS, and radiosondes
 468 at ARM site, *J. Geophys. Res. Atmos.*, 119, 9596-9613, <https://doi.org/10.1002/2014JD021730>, 2014.

469 Pérez-Ramírez, D., Smirnov, A., Pinker, R. T., Petrenko, M., Román, R., Chen, W., Ichoku, C., Noël, S., Abad, G. G., Lyamani,
 470 H., and Holben, B. N.: Precipitable water vapor over oceans from the Maritime Aerosol Network: Evaluation of global
 471 models and satellite products under clear sky conditions, *Atmos. Res.*, 215, 294-304,
 472 <https://doi.org/10.1016/j.atmosres.2018.09.007>, 2019.

473 Prasad, A. K. and Singh, R. P.: Validation of MODIS Terra, AIRS, NCEP/DOE AMIP-II Reanalysis-2, and AERONET Sun
 474 photometer derived integrated precipitable water vapor using ground-based GPS receivers over India, *J. Geophys. Res.*
 475 *Atmos.*, 114, D05107, <https://doi.org/10.1029/2008JD011230>, 2009.

476 Qin, J., Yang, K., Koike, T., Lu, H., Ma, Y. M. and Xu, X. D.: Evaluation of AIRS precipitable water vapor against ground-
 477 based GPS measurements over the Tibetan Plateau and its surroundings, *J. Meteorol. Soc. Jpn.*, 90, 87-98,
 478 <https://doi.org/10.2151/jmsj.2012-C06>, 2012.

479 Rakesh, V., Randhir, S., Pal, P. K., and Joshi, P. C.: Impacts of satellite-observed winds and total precipitable water on WRF
 480 short-range forecasts over the Indian region during the 2006 summer monsoon, *Wea. Forecasting*, 24, 1706-1731,

481 <https://doi.org/10.1175/2009WAF2222242.1>, 2009.

482 Sobrino, J. A., Juan, C. J., Cristian, M. and Guillem, S.: Evaluation of Terra/MODIS atmospheric profiles product (MOD07)

483 over the Iberian Peninsula: a comparison with radiosonde stations, *Int. J. Digit. Earth*, 8(10), 1-13,

484 <https://doi.org/10.1080/17538947.2014.936973>, 2014.

485 Solbrig, J. E.: Thin cloud length scales using CALIPSO and CloudSat data, M.S. thesis, Department of Atmospheric Sciences,

486 Texas A&M University, Texas, U.S.A, 62 pp., 2009.

487 Trenberth, K. E., Dai, A. G., Rasmussen, R. M., and Parsons, D. B.: The changing character of precipitation, *B. Am. Meteorol.*

488 *Soc.*, 84(9), 1205-1218, <https://doi.org/10.1175/BAMS-84-9-1205>, 2003.

489 Turner, D. D., Lesht, B. M., Clough, S. A., Liljegren, J. C., Revercomb, H. E., and Tobin, D. C.: Dry Bias and Variability in

490 Vaisala RS80-H Radiosondes: The ARM Experience, *J. Atmos. Ocean. Tech.*, 20, 117-132, [https://doi.org/10.1175/1520-](https://doi.org/10.1175/1520-0426(2003)020<0117:DBAVIV>2.0.CO;2)

491 [0426\(2003\)020<0117:DBAVIV>2.0.CO;2](https://doi.org/10.1175/1520-0426(2003)020<0117:DBAVIV>2.0.CO;2), 2003.

492 Wang, L., Hu, X. Q., Xu, N., and Chen, L. Water vapor retrievals from near-infrared channels of the advanced Medium

493 Resolution Spectral Imager instrument onboard the Fengyun-3D satellite, *Adv. Atmos. Sci.*,

494 <https://doi.org/10.1007/s00376-020-0174-8>, 2021.

495 Wang, J. H., Dai, A. G., and Mears, C.: Global water vapor trend from 1988 to 2011 and its diurnal asymmetry based on GPS,

496 radiosonde, and microwave satellite measurements, *J. Climate*, 29(14), 5205-5222. [https://doi.org/10.1175/JCLI-D-15-](https://doi.org/10.1175/JCLI-D-15-0485.1)

497 [0485.1](https://doi.org/10.1175/JCLI-D-15-0485.1), 2016.

498 Wang, J. H., Zhang, L. Y., Dai, A. G., Hove, T. V., and Baelen, J. V.: A near-global, 2-hourly data set of atmospheric

499 precipitable water from ground-based GPS measurements, *J. Geophys. Res. Atmos.*, 112, D11107.

500 <https://doi.org/10.1029/2006JD007529>, 2007.

501 Wang, S. M., Xu, T. H., Nie, W. F., Jiang, C. H., Yang, Y. G., Fang, Z. L., Li M. W., and Zhang Z.: Evaluation of precipitable

502 water vapor from five reanalysis products with ground-based GNSS observations, *Remote Sens.*, 12(11), 1817,

503 <https://doi.org/10.3390/rs12111817>, 2020.

504 Westwater, E. R.: The accuracy of water vapor and cloud liquid determination by dual-frequency ground-based microwave

505 radiometry, *Radio Sci.*, 13(4), 677-685, <https://doi.org/10.1029/RS013i004p00677>, 1978.

506 Wu, R. H., Zhang, P., Xu, N., Hu, X. Q., Chen, L., Zhang, L., and Yang, Z. D.: FY-3D MERSI on-orbit radiometric calibration

507 from the lunar view, *Sensors*, 20(17), 4690, <https://doi.org/10.3390/s20174690>, 2020a.

508 Wu, Z., Liu, Y., Liu, Y., Wang, J., He, X., Xu, W., Ge, M., and Schuh, H.: Validating HY-2A CMR precipitable water vapor

509 using ground-based and shipborne GNSS observations, *Atmos. Meas. Tech.*, 13, 4963–4972, [https://doi.org/10.5194/amt-](https://doi.org/10.5194/amt-13-4963-2020)

510 [13-4963-2020](https://doi.org/10.5194/amt-13-4963-2020), 2020b.

511 Xu, N., Niu, X. H., Hu, X. Q., Wang, X. H., Wu, R. H., Chen, S. S., Chen, L., Sun L., Ding L., Yang Z. D., and Zhang, P.: Prelaunch calibration and radiometric performance of the advanced MERSI II on FengYun-3D, *IEEE T. Geosci. Remote*,

512 *Sens.*, 56, 4866-4875, <https://doi.org/10.1109/TGRS.2018.2841827>, 2018.

513

514 Yang, Z. D., Zhang, P., Gu, S. Y., Hu, X. Q., Tang, S. H., Yang, L. K., Xu, N., Zhen, Z. J., Wang L., Wu, Q., Dou, F. L., Liu, R.

515 X., Wu, X., Zhu, L., Zhang, L. Y., Wang, S. J., Sun, Y. Q., and Bai, W. H.: Capability of Fengyun-3D satellite in earth

516 system observation, *J. Meteorol. Res.-PRC.*, 33(6), 1113-1130, <https://doi.org/10.1007/s13351-019-9063-4>, 2019.

517 Zhao, T. B., Dai, A. G., and Wang, J. H.: Trends in tropo-spheric humidity from 1970 to 2008 over China from a homogenized
 518 radiosonde dataset, *J. Climate*, 25, 4549-4567, <https://doi.org/10.1175/jcli-d-11-00557.1>, 2012.
 519 Zhang, F. Z., Barriot, J.-P., Xu, G. C., and Yeh, T.-K.: Metrology assessment of the accuracy of precipitable water vapor
 520 estimates from GPS data acquisition in tropical areas: the Tahiti case, *Remote Sens.*, 10 (5), 758,
 521 <https://doi.org/10.3390/rs10050758>, 2018.
 522 Zhang, J. Q., Chen, H. B., Li, Z. Q., Fan, X. H., Peng, L., Yu, Y., and Cribb, M.: Analysis of cloud layer structure in Shouxian,
 523 China using RS92 radiosonde aided by 95 GHz cloud radar, *J. Geophys. Res. Atmos.*, 115, D00K30,
 524 <https://doi.org/10.1029/2010JD014030>, 2010.
 525 Zhang, W. G., Xu, G. R., Wan, R., He, W. H., and Feng, G. L.: Analysis of the characteristic of liquid water and water vapor
 526 detected by ground-based microwave radiometer, *Torrential Rain and Disasters*, 34 (4), 367-374, 2015. (in Chinese with
 527 English abstract)